A Moored Array Observation Dataset for Air-Sea·Surface and Ocean in the Northern South China Sea during 2014–2015 (MASCS 1.0)

Han Zhang[1,2,3*], Dake Chen[1,2,4], Tongya Liu[1,2], Di Tian[1], Min He[2], Qi Li[2], Guofei Wei[6,7], Jian Liu[2,5]

Correspondence: Han Zhang (zhanghan@sio.org.cn)

[1] State Key Laboratory of Satellite Ocean Environment Dynamics, Second Institute of Oceanography, Ministry of Natural Resources, Hangzhou 310012, China

[2] Southern Marine Science and Engineering Guangdong Laboratory (Zhuhai), Zhuhai 519082, China

[3] State Key Laboratory of Marine Environmental Science, Xiamen University, Xiamen 361102, China

[4] School of Oceanography, Shanghai Jiao Tong University, Shanghai 200030, China

[5] School of Geography and Ocean Science, Ministry of Education Key Laboratory for Coast and Island Development, Nanjing University, Nanjing 210023, China

[6] Key Laboratory of Straits Severe Weather China Meteorological Administration, Fuzhou 350028, China

[7] Fujian Meteorological Observatory, Fuzhou 350028, China

Abstract. This study reports a moored array dataset (MASCS 1.0) consisting of five buoys and four moorings in the northern South China Sea during 2014–2015. The dataset includes measurements of sea surface meteorological data using two sets of instruments, sea surface waves measured by a wave recorder, temperature and salinity from the surface to a depth of 400 m, and at 10 m and 50 m above the ocean bottom by conductivity, temperature, and depth (CTD) recorders. It also includes currents from the surface to a depth of 850 m measured by acoustic Doppler current profilers (ADCPs) and at 10 m, 50 m, and 100 m above the floor measured by current meters. Additional measurements were taken for sea surface radiation, air visibility, chlorophyll, turbidity and chromophoric dissolved organic matter at Buoy 3, which was located at the center of the moored array. The data reveals air-sea interactions and oceanic processes in the upper and bottom ocean, especially the transition of air-sea interface and ocean conditions from summer to winter monsoon along with the effects of six tropical cyclones on the moored array. The multiscale processes such as air-sea fluxes, tides, internal waves and low-frequency flows were also recorded. The data is valuable and has multiple potential applications, including analysis of the phenomena and mechanisms

of air-sea interactions and ocean dynamics, as well as validation and improvement of numerical model simulations, data reanalysis and assimilations. All the data described here are made publicly available from https://zenodo.org/records/13827819 (Zhang et al. 2024).

1 Introduction

The South China Sea (SCS) is a semi-enclosed marginal sea with a deep basin, making it the largest marginal sea in the tropics, covering nearly 3.5×10^6 km^2. The South China Sea is also the largest marginal sea in the western Pacific, known for its powerful internal tides and abundant internal waves (Alford et al., 2015). Mesoscale eddies in the SCS transport heat and salt from Kuroshio loop near the Luzon Strait (Yang et al., 2019) and modulate sea surface fields (Tan et al., 2023). The background circulations in the SCS are cyclonic in the upper and deep layers, while they are anticyclonic in the middle layer (Cai et al., 2020). The three factors contributing to the generally cyclonic gyre in the upper ocean of the northern SCS (Jilan, 2004; Liu et al., 2008) are: (1) quasi-seasonal wind forcing; (2) net water transport into the SCS through the Luzon Strait; and (3) vorticity advection from the Kuroshio. The Kuroshio carrying the northwestern Pacific water intrudes into the SCS through the Luzon Strait (Nan et al., 2015).

The SCS is significantly influenced by atmospheric forcing, such as monsoons (Chen et al., 2023; Chen et al., 2022), tropical cyclones (TCs) (Guan et al., 2024; Shan et al., 2023), and the world's strongest boreal summer quasi-biweekly oscillation (Qi et al., 2023). Marine heat waves (Wang et al., 2022) and variations in air-sea heat flux (Song et al., 2023; Zhang, 2023) are also observed in the northern SCS. This sector features broad continental shelves and steep continental slopes, leading to complex local ocean dynamical processes. For example, breaking internal tides on the continental slope induce along-slope deep sea bottom currents (Xie et al., 2018), and cross-isobathic motion of the water column or synoptic processes (e.g., TCs) induce continental shelf waves, such as topographic Rossby (Wang et al., 2019) and Kelvin mode (Li et al., 2024) waves.

Owing to the complexity of air-sea interaction and oceanic processes in the SCS, local in-situ observations are essential to uncover the phenomena and mechanisms. From 2014 to 2015, a moored array consisting of five buoys and four moorings was deployed in the northern SCS to acquire sea surface meteorological and oceanic data as well as upper and near-bottom oceanic data. This study lists the details of these observations and the resulting dataset. Part of this data have already been used in several studies focusing on air-sea heat flux, ocean temperature-salinity, and dynamical responses to tropical cyclones (Zhang et al., 2016; Zhang et al., 2018; Liu et al., 2020; Zhang, 2023), to investigate the effect of drag coefficients on surface heat flux during typhoon (Liu et al. 2022), the influence of typhoons on the pre-existing eddies (He et al., 2024), ocean mixing and heat flux by near-inertial waves (Hong et al. 2022; Lu et al., 2024), sea surface wind patterns (Zhang et al., 2020) and the comparison of microseisms signals generated by typhoons (Lin et al., 2022), the validity of numerical model simulations (Wu et al., 2020; Lim Kam Sian et al., 2020; Lu et al., 2023), and the study of deep ocean energy variability in the SCS (Quan et al., 2022). However, the full potential of this dataset has yet to be realized.

2 Moored array observations

2.1 Positions of buoys and moorings

The observation array consisted of five buoys (B1-B5) and four moorings (M1, M2, M4, M5) in the northern South China Sea (Figs. 1 and 2), deployed from June to September 2014 and recovered from September 2014 to March 2015 (Table 1). The water depth at buoy 1 (B1) and mooring 1 (M1) was approximately 1600 m, while the depths at other stations were greater than 3000 m. Tropical cyclones significantly influenced the observations, as shown in Fig. 1, including Hagibis in June, Rammasun and Matmo in July, Kalmaegi and Fung-wong in September, and Hagupit in December. The information regarding these tropical cyclones was obtained from the China Meteorological Administration (https://tcdata.typhoon.org.cn/en/zjljsjj.html), which were deemed more accurate for tropical cyclones affecting China (Lu et al., 2021; Ying et al., 2014). Although the design of some buoys and moorings have already been shown in previous works (e.g. Zhang et al., 2016; Zhang, 2023), the designs of all the stations are redrawn to give more accurate information of the deployment of the instruments (Fig. 1b, Fig. 3).

Table 1 shows the locations of the observation stations as well as their time range. The moorings (M1, M2, M4, M5) were deployed during 8 to 10 June 2014 and successfully recovered during 29 to 31 March 2015 (Table 1). B1 was deployed on 19 June 2014, maintained once on 5 September 2014, it lost contact on 15 October while did not recover by two cruises during 23 March to 4 April 2015. Buoy 2 (B2) and 4 (B4) deployed on 29 July and 20 June 2014, while recovered on 30 March 2015. B4 was maintained once on 30 July 2014. Buoy 3 (B3) was deployed on 11 September, the tether of B3 snapped on 15 September 2014, when typhoon Kalmaegi passed over the observation array (Zhang et al., 2016). B3 then became a drifter, initially moving northeastward with circular tracks (Fig. 2a) attributed to the rightward advection and near-inertial surface currents induced by the typhoon. B3 returned to its initial location on 21 September 2014, moved eastward and turned back on 25 September 2014, and followed a southwestward track thereafter (Fig. 2a). B3 was recovered by a ship on 17 October 2014 and it was brought back to land on 21 October 2014. Moored part of B3 was recovered on 31 March 2015. Buoy 5 (B5) was deployed on 26 August 2014, lost contact on 11 October 2014, while the moored part of B5 was recovered on 31 March 2015. The horizontal movement of the buoys was minimal during observations, as they primarily moved in a circular region with a radius shorter than 3 km (Figs. 2b-e). Typhoon Kalmaegi also increased the horizontal circular movement of B1 to approximately 4 km on the northwest side on 15 September, which was attributed to the northwestward winds on the right side of the typhoon and may indicate that the anchor of B1 was northwestward moved by the typhoon as its tether length was approximately 2 km (nearly half of 4 km), see Figs. 2c and 3a.

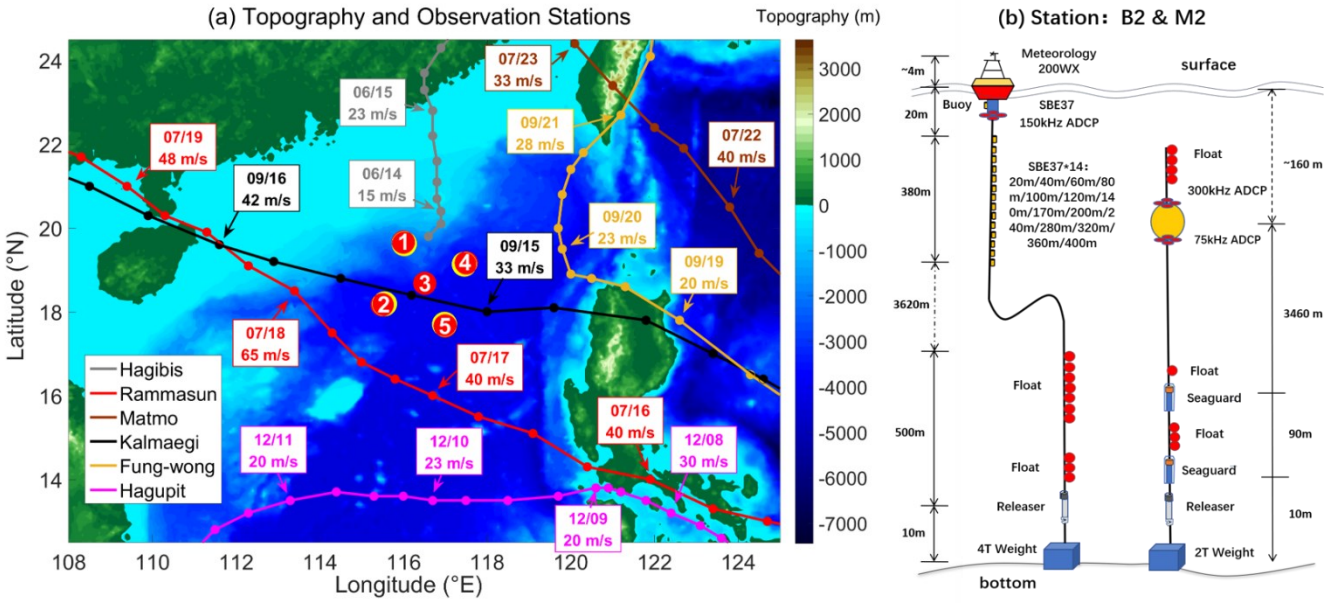

90 **Figure 1: (a): Topography (m) map with the positions of and the deployed locations of buoys (red dots) and moorings (yellow dots). (b) Designs of buoy 2 (B2) and mooring 2 (M2) are shown as examples, dot-and-dash line indicates the tether length in middle water of the buoy, while dashed line indicates depth of the two ADCPs on the top of the mooring. Tracks of tropical cyclones are shown (colored lines), along with their positions every 6 h (dots). The text boxes indicate the dates and sustained maximum wind speed at UTC 00:00 on each date.**

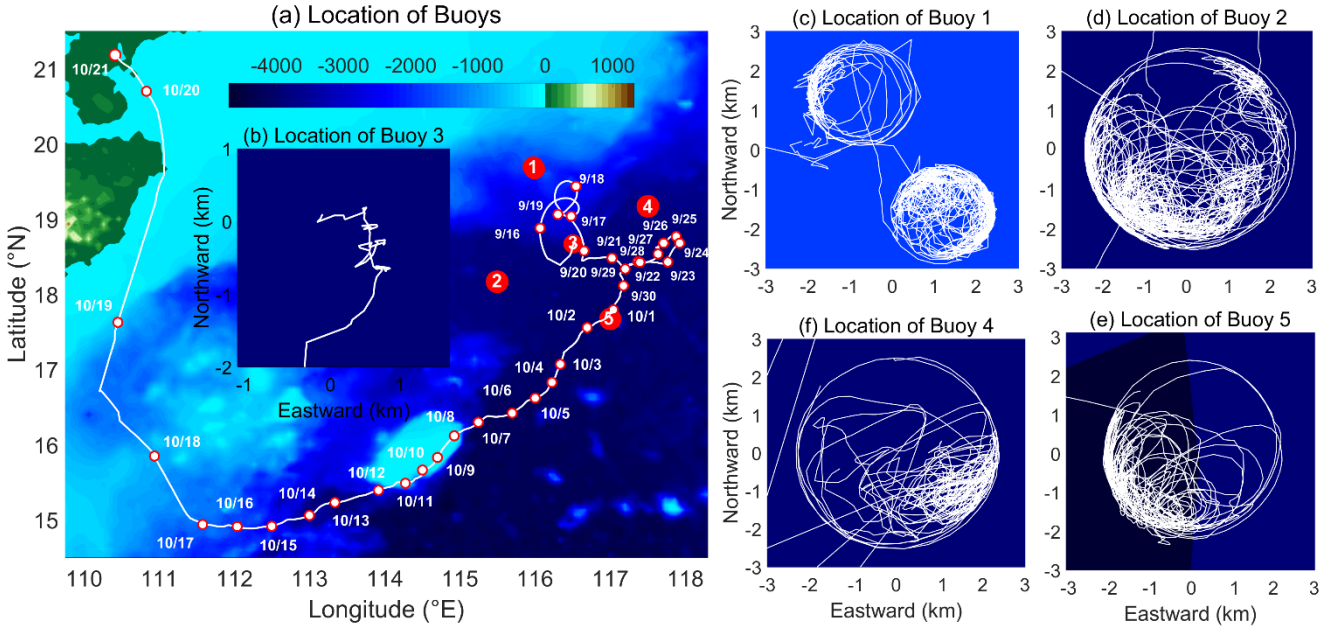

95 **Figure 2: (a): Distributions of the buoy locations, with the track of buoy 3 (B3). (b-e): Tracks of buoy 3, 1, 2, 4 and 5 (B3, B1, B2, B4 and B5) with their locations relative to their initial deployed positions in northward and eastward directions (km). White lines represent the buoy tracks, while white hollow dots indicate the positions of B3 every day after 15 September 2014 when its tether snapped and became a drifter.**

Table 1. Information of the observation station

Station	Deployed Longitude (E)	Deployed Latitude (N)	Estimated Water Depth (m)	Time Range*
Buoy 1 (B1)	115°59’49.8”	19°40’04.8”	1625	2014.06.19–2014.10.15
Buoy 2 (B2)	115°29’53.5”	18°09’59.3”	3710	2014.07.29–2015.03.30
Buoy 3 (B3)	116°30’33.9”	18°40’40.2”	3310	2014.09.11–2014.10.17
Buoy 4 (B4)	117°30’11.4”	19°10’01.7”	3430	2014.06.20–2014.03.30
Buoy 5 (B5)	116°59’55.7”	17°39’58.8”	3930	2014.08.26–2015.03.31
Mooring 1 (M1)	116°01’17.1”	19°37’28.7”	1630	2014.06.08–2015.03.29
Mooring 2 (M2)	115°32’57.8”	18°11’29.5”	3740	2014.06.10–2015.03.30
Mooring 4 (M4)	117°27’16.8”	19°08’24.9”	3410	2014.06.09–2015.03.30
Mooring 5 (M5)	116°58’50.8”	17°42’18.1”	3930	2014.06.10–2015.03.31

***B1 were lost and not recovered, the end time of B1 represents the latest time when observation data received. Otherwise, time range represents the deployment and recovery time for the stations.**

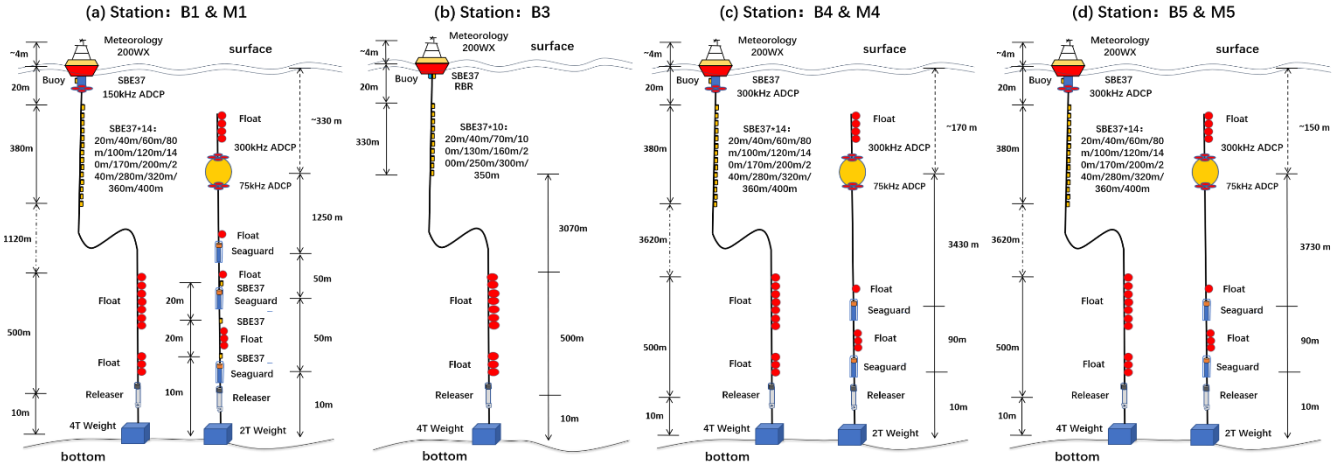

Figure 3: Design of stations 1, 3, 4, and 5. Note that all the stations consist of both a buoy and a mooring, except station 3, which only has a buoy. The dot-and-dash lines indicate the tether length in middle water of the buoy, while dashed lines indicate depth of the two ADCPs on the top of the mooring.

Table 2. Observation data details at each station

	Stations	Recorded Data	Equipment and Position	Time Resolution
Buoy Location 1	B1-B5	Longitude (°E), Latitude (°N)	GPS sensor 1	1 h
Buoy Location 2			GPS sensor 2	
Buoy Location 3	B1, B2, B4, B5		GPS sensor 3	1 h (B1, B4), 3 h (B2) or 6 h (B5)
Meteorological data 1	B1-B5	Air temperature (°C), Air pressure (hPa), Relative humidity (%),	Meteorological sensors at 4 m height from sea surface	

Meteorological data 2		Compass (°), Wind speed (m/s, average and maximum), Wind direction (°, average and maximum), Rain guage (mm), Compass (°)	Auto meteorological station (200WX) at 4 m height from sea surface	12 min (B2) or 1 h (B1, B3, B4, B5)
Current 1*	B1, B2, B4, B5, M1, M2, M4, M5	Speed (cm/s), Direction (°), Vertical velocity (cm/s), Temperature, Bin (m), Real-time and designed depth of the ADCP (m, Depth and Depth 0)	Downward looking for ADCP 1, 3, and uplooking for ADCP 2	3 min (300 and 150 kHz ADCP) or 15 min (75 kHz ADCP)
Current 2	M1, M2, M4, M5	Speed (cm/s), Direction (°)	SeaGuard at 10 m (M1, M2, M4, M5), 50 m (M1) and 100 m (M1, M2, M4, M5) from ocean bottom	10 min
Sea temperature, salinity and pressure	B1, B2, B4, B5, M1	Temperature (°C), Salinity (psu), Pressure (dbar), Depth (m)	SBE-37 with design depth (m) at buoys: 20, 40, 60, 80, 100, 120, 140, 170, 200, 240, 280, 320, 360, 400. SBE-37 with design depth 10 m and 50 m above the bottom at M1	2 min
Sea Surface Waves	B1, B4	Wave height (m, Significant and Maximum), Peak period (s), Mean wave direction (°), Wave spread	Wave gauge at sea surface (0 m)	1 h
Radiation (W/m^2)	B3	Short wave (upward, downward), Long wave (upward, downward), Air temperature (°C)	Wave radiometer at 4 m height from sea surface	1 h
Visibility (VIS, km)		Air visibility (km)	Visibility meter at 4 m height from sea surface	
Biochemistry data		Water pressure (dbar), Turbidity (V, two sensors), Chlorophyll (ug/L, Chla), Colored dissolved organic matter (ppb, CDOM)	RBR sensors at sea surface (0 m)	12 min

*ADCP 1 was the downward looking ADCP deployed at buoy, ADCP 2 and 3 were the upward and downward looking ADCPs on the mooring. 300 kHz ADCPs were binned in 4 m with the first bin at 8 m (B4) or 6.24 m (M1, M2) and the last bin at 124 m (B4) or 122.24 m (M1, M2). 150 kHz ADCPs were binned in 8 m with the first bin at 14 m and the last bin at 246 m. 75kHz ADCP binned in 16 m intervals with the first bin at 24.7 m and the last bin at 568.7 m. ADCP 1 at B5 was lost during observation and no data recovered.

2.2 Dataset description

The dataset is composed of 52 files in netcdf file (.nc) format containing air and ocean observation data as well as the positions of the buoys during the period of 2014–2015, along with a metadata file in .txt format to give a brief introduction of the data. The observation instruments were calibrated before deployment and the observation data are transformed directly to

netcdf files after output from the observation instruments, with the units and FillValues labeled. No special modification or say quality control was applied in order to keep the original output data unchanged. All the files include time values both Coordinated Universal Time (UTC) and local time which is eight hours ahead of the Coordinated Universal Time (UTC +8) since 0000-01-01 00:00:00. The local time is also called China Standard Time (CST) or Beijing Time (BJT). The location data includes longitude (°E) and latitude (°N) observed by Global Positioning System (GPS) sensors. There were three GPS sensors on buoys 1, 2, 4, and 5, and two GPS sensors on buoy 3. Location-1 data was obtained from the main GPS sensors on the body of the buoys, Location-2 data was obtained from the GPS sensors approximately 4 m above the sea surface, and Location-3 data was obtained from the low-frequency GPS sensors at the bottom of the buoys (approximately 0 m). The measurement accuracies of the GPSs were <50 m.

The air data includes observations approximately 4 m above the sea surface from meteorological sensors (Meteorology data) and the automatic meteorological station (200WX data). In Two sets of meteorological stations are deployed on the buoys in order to have a backup in case when sensors of a meteorological station break down during observation. The 200WX data are similar to the meteorology data, but does not include rain guage data. The direction of wind indicates the direction of the incoming wind; for example, 0° indicates wind passing from north to south, and 90° indicates wind passing from east to west. The compass indicates the direction of the compass on the meteorological sensors or stations, which refers to the attitude of the sensors or stations. For the measurement accuracies of 200WX, the air pressure is ±1 hPa air temperature accuracy is ± 1.1 °C, the relative humidity is ±5 %, the compass is 1° for static heading and 2° for dynamic heading, while the measurement accuracy of wind is different in dry and wet conditions. In dry condition, the wind speed accuracy is 0.5 m/s + 10% of reading for low winds (0 to 5 m/s), or the greater value of 1 m/s or 10% for high winds (5 to 40 m/s), the wind direction accuracy is 5° for low winds (2 to 5 m/s) and 2° for high winds (＞5 m/s). In wet condition, the wind speed accuracy is 2.5 m/s and 8°. The measurement accuracy of meteorological sensors has same order with 200WX. For the meteorology data of buoy 3, there was a visibility meter to measure air visibility (km), while also a Campbell Scientific NR01 four-component net radiometer approximately 4 m above the sea surface with outputs every 1 h, measured upward and downward shortwave and longwave radiation (W/m^2) as well as air temperature observed by the radiometer (°C). The measurement accuracy ± 10% of the measurement range for air visibility, ＜2.4 % the measurement range for shortwave radiation and ＜7 % for longwave radiation.

The ocean data includes sea surface waves observed by TRIAXYS^{TM} OEM wave recorder (Wave data), temperature, salinity, and pressure (CTD) observed by Sea-Bird Scientific 37 recorders (SBE data), currents observed by Teledyne RD Instruments (TRDI) acoustic doppler current profilers (ADCP data) and currents observed by Aanderaa Data Instruments SeaGuard Recording Current Meter (SeaGuard data), and Biochemistry data observed by multi-parameter Richard Brancker Research sensors (RBR data). The 75 kHz ADCP was TRDI Workhorse Long Ranger, 150 kHz ADCP was TRDI Workhorse Quartermaster and 300 kHz ADCP was TRDI Workhorse Sentinel. Sea surface wave data includes significant wave height (m), maximum wave height (m), mean wave direction (°), peak period (s), and wave spread (Table 2). The observation accuracy is better than 2% of the measurement range for pressure for wave height and period, while ±1° for wave direction. Wave

recorders were deployed on buoys 1, 4, and 5, but the wave recorder on buoy 5 broke down, resulting in low-quality data. Consequently, only sea surface wave data from buoys 1 and 4 were included in the ocean data. SBE data includes temperature (°C), salinity (psu), and pressure (dbar) observed by SBE-37 CTD sensors. The measurement accuracies of SBE-37 is ± 0.002 °C (-5 to 35 °C) or ±0.01 °C (35 to 45 °C) for temperature, ±0.0003 S/m for electrical conductivity and 1% of the measurement range for pressure. Serial 1 to 15 in the SBE data refers to the SBE-37 sensors from the surface to the ocean bottom. All SBE sensors are deployed on the buoys, except for three SBE-37s on the moorings located near the ocean bottom (Figs. 1b and 2). Note that the SBE-37 strings on buoys 1 and 3 were lost during deployment period, so only SBE data at the sea surface located at the bottom of the buoy (Temperature1, Salinity1, and Pressure1) was obtained. Two SBEs on buoy 4 broke down during observation, resulting in data from only 13 SBEs. The ADCP data consists of current speed (cm/s Speed), current direction (° direction), temperature observed by ADCP (°C temperature), depth of the ADCP (m depth), designed depth (depth0), and bin intervals of the ADCP observation (m bin). The SeaGuard data includes current speed (cm/s speed) and current direction (° direction). Unlike wind direction, current direction indicates the direction of the current flow, for example, 0° indicates current passing from south to north, and 90° indicates the current passing from west to east. In SeaGuard data, the accuracy is ±1° of reading for current speed, while ±3° (if tilt is 0-15°) or ±5° (if tilt is 15-35°) for current direction. Negative Bin values refer to downward-looking ADCPs and vice versa. ADCPs on the buoys (ADCP 1) were downward-looking, located at the sea surface (approximately 0 m), so their observation range was depth0 + bin. The ADCP data on moorings consist of upward-looking (ADCP 2) and downward-looking (ADCP 3) observations with ranges depth + Bin, as the depth of the ADCPs at moorings varies during observation. Note that buoy 3 did not have ADCP or SeaGuard observation (see Fig. 3 and Table 2), and ADCP at buoy 5 broke down and no data obtained. For the bin sizes of ADCPs, 300 kHz ADCPs were binned in 4 m with the first bin at 8 m (buoy 4) or 6.24 m (mooring 1 and 2) and the last bin at 124 m (buoy 4) or 122.24 m (mooring 1 and 2). 150 kHz ADCPs were binned in 8 m with the first bin at 14 m and the last bin at 246 m. 75kHz ADCP binned in 16 m intervals with the first bin at 24.7 m and the last bin at 568.7 m. The velocity accuracy for 75 kHz ADCP is 1% of water velocity relative to the ADCP ±0.01 m/s (written as 1%±0.01 m/s), while the accuracies for 150 and 300 kHz ADCP are 1%±0.005 m/s and 0.5%±0.005 m/s, respectively. The RBR sensors were only deployed at buoy 3, observed water pressure (dbar), turbidity (V) by two sensors, chlorophyll (ug/L Chla) and Colored dissolved organic matter (ppb CDOM). The measurement accuracy of water pressure was ±0.05 % of measurement range for water pressure, ±2% of the measurement range for turbidity and chlorophyll, ±0.01 ppb for CDOM,

3 Results

The data at station 2 (B2 and M2) were long and more complete relative to other stations, and is shown first to provide an example of the observations at the stations. Subsequently, observations differing from station 2 are also shown, including near-bottom observations at B1, sea surface waves at B1 and B4, and the observations at B3 after its rope snapped on 15 September, causing it to become a drift.

3.1 Sea surface air and ocean observation at station 2

The prevailing wind direction was approximately 200° (nearly south wind) from late July to mid-August, then shifted primarily in the range of 20°–80° (nearly northeast wind) after October, with wind direction variations during September (Fig. 4b,d). This finding indicates that the transition occurred from local summer to winter monsoon, with September as the transition month. Average wind speed is less than 10 m/s during July and August, often exceeding 10 m/s after October (Fig. 4a,c), indicating that the winter monsoon was stronger than the summer monsoon at B2. B2 likely traveled through the eye of typhoon Kalmaegi, with two peaks in wind speed accompanied by minimum air pressure (Zhang et al., 2016). Note that typhoon Kalmaegi and severe tropical storm Fung-wong during September significantly influenced wind direction at B2, with wind direction turning counter-clockwise near September 15 and 21, consistent with B2 being on the left side of both TCs.

B2 also recorded a drop in sea surface air and ocean temperature (Fig. 4g,i) from summer to winter, ranging from approximately 28.5 °C to 30.5 °C in August, decreasing from approximately 29 °C to approximately 27 °C in October, and continuing to decrease further. Surface air temperature was slightly lower than sea surface temperature during the observation period, indicating local sensible heat flux from the ocean to the atmosphere, as water cooled slower than air during autumn. The diurnal variation of temperature, attributed to daytime solar radiation heating and nighttime outward longwave radiation cooling, and the deepening of the ocean mixed layer, were also captured by the observations due to their high time resolution (2 min). Typhoon Kalmaegi and Fung-wong successively decreased sea surface air and ocean temperatures during September, with Kalmaegi suddenly decreasing sea surface temperature by approximately 2.5 °C, as B2 was located in the core cooling area on the right side of the typhoon track.

Rain guage data was measured by a tipping bucket rain gauge, with a maximum measurement of 255 mm. The bucket empties when full (255 mm) and measurement starts from 0 mm again. Rain rate can be calculated by dividing the difference in rain guage values by the time interval. Significant rainfall events were recorded near 2 August, 6 September, 15 September, and 21 September. The strong rainfall near 15 September and 21 September was induced by typhoon Kalmaegi and severe tropical storm Fung-wong. Note that evaporation also affected rain guage values, which decreased slowly over time without precipitation, indicating that rain guage data reflected precipitation and evaporation. Sea surface salinity increased from approximately 33.3 psu near 1 October to approximately 33.8 psu near 10 November (Fig. 4i), owing to little rainfall during this period, with salinity primarily controlled by evaporation.

There were some consistencies and differences between the two sets of meteorological observations, European Centre for Medium-Range Weather Forecasts (ECMWF) Reanalysis v5 data (ERA5, https://www.ecmwf.int/en/forecasts/dataset/ecmwf-reanalysis-v5) is used to evaluate the performance of them. The average and maximum wind speed and direction in the Meteorology and 200WX datasets are consistent while average wind matched wind speed from ERA5 well, except that average wind direction observed by meteorological sensors suddenly turned to approximately 180° and maximum wind direction varied rapidly between 0° and 360° after 15 November (Fig. 4b,d), indicate some malfunctions of the wind meteorological observation sensor. Air pressure measurements from the

meteorological sensors, 200WX station and ERA5 are consistent before 27 August, with the diurnal variation of air pressure observed by the meteorological sensors amplifying and becoming inconsistent with 200WX observations and ERA5 after 27 August (Fig. 4f), indicate some malfunction of the pressure meteorological observation sensor. The sensitivity of air temperature measurements by the 200WX was greater than the temperature meteorological sensor with larger amplitude diurnal variations, while values of both of them a bit greater or different with ERA5 data (Fig. 4g). Relative humidity measured by the meteorological sensor was consistent with ERA5 data and was greater than that measured by the 200WX, ranging from 0 % to 10 % (Fig. 4h). Both two sets of meteorological observations showed missing data about 5 days near 6 October, which may due to the malfunction of the instruments or data recording.

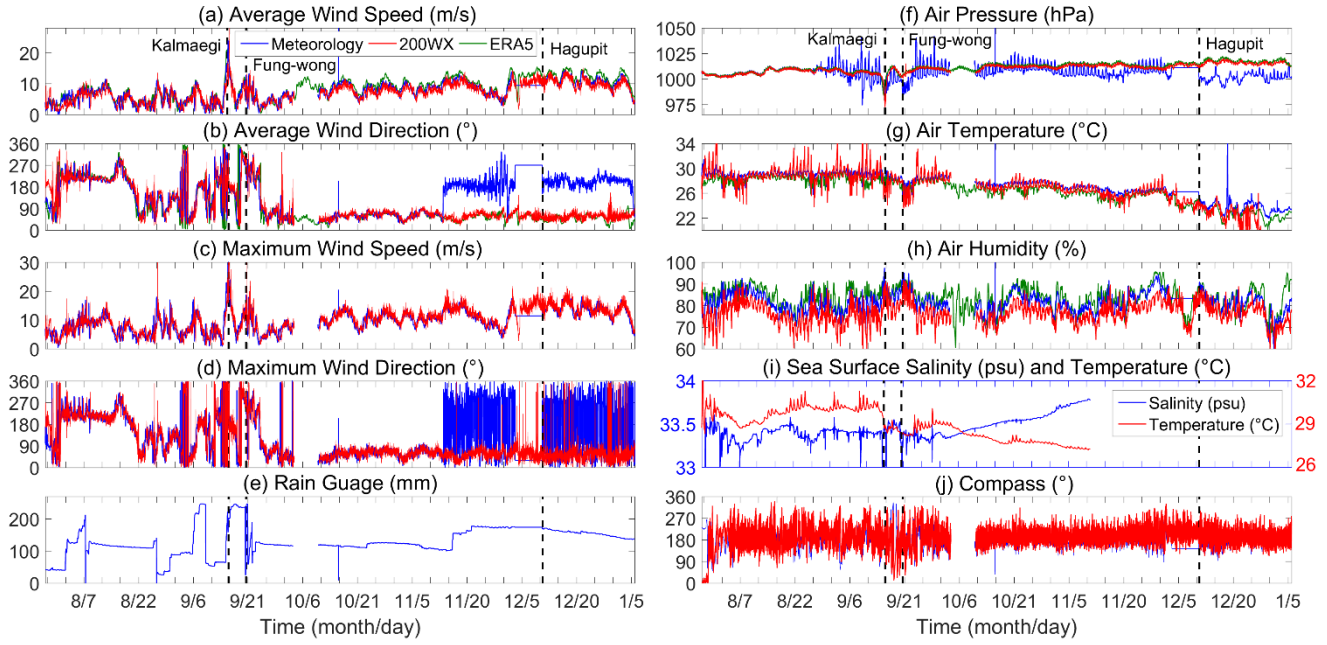

Figure 4: Observation at Buoy 2. Average and maximum wind speed (a, b m/s) and direction (c, d °), rain guage (e mm), air pressure (f hPa), air temperature (g °C), relative humidity (h %), sea surface salinity (i psu), sea surface temperature (i °C), and buoy compass (j °). Blue and red lines are data observed by meteorological sensors and the 200WX automatic meteorological station, approximately 4 m above the sea surface, while blue and red lines in (i) represent salinity and temperature observed by the SBE-37 sensor at the buoy bottom (approximately 0 m). Wind directions indicate the direction from which the wind originates. The vertical dashed lines indicate the time when TC Kalmaegi, Fung-wong and Hagupit closest to Buoy 2. The green lines are European Centre for Medium-Range Weather Forecasts (ECMWF) Reanalysis v5 (ERA5) data.

3.2 Current, temperature, and salinity observation at station 2

At station 2, the current observations at the mooring (Fig. 5b–d) were longer than those at the buoy (Fig. 5a), as well as the temperature and salinity (Fig. 6) observations at the buoy, due to the deployment and recovery times. The upward-looking 300 kHz ADCP (Fig. 5b) and the SBE-37 recorder at the bottom of the buoy (Fig. 6) stopped working near 11 November, while data quality from the downward-looking 75 kHz ADCP at the mooring decreased especially in year 2015, with some missing data at several bins (Fig. 5b). Although the length of the chain of SBEs was 400 m, the observation range of

temperature and salinity was primarily shorter than 400 m, as the rope swung and tilted during observation, especially the deepest observation depth decreased to ~200 m near 21 September under the influence of typhoon-induced near-inertial waves after Kalmaegi. Similarly, the positions of ADCPs at moorings also moved vertically due to the tilt of the mooring rope, especially when influenced by intensified currents after Rammasun and Matmo in July, Kalmaegi in September.

Horizontal currents induced by diurnal and semi-diurnal tides were captured by ADCPs and SeaGuards, along with diurnal and semi-diurnal vertical variations of temperature and salinity isolines. The upper ocean background current speed was primarily <20 cm/s, significantly increasing after tropical cyclones, e.g., Rammasun and Matmo in July, Kalmaegi in September, and Hagupit in December, with mixed layer current speed reaching approximately 150 cm/s after Kalmaegi (Zhang et al., 2016). Typhoon Kalmaegi immediately strengthened near-inertial mixed layer currents and kinetic energy, which then propagated horizontally and vertically with the dispersion of near-inertial waves and regulation by background vorticity (Lu et al., 2023; Lu et al., 2024; Zhang et al., 2016). Near-bottom currents were mainly <10 cm/s, while near-bottom flow turned from northeastward to southeastward after the influence of typhoon Rammasun.

Upper ocean temperature decreased monotonously from the surface (approximately 0 m) to approximately 400 m, and salinity exhibited a "low-high-low" vertical structure with a maximum of approximately 34.5 psu from approximately 100 m to approximately 250 m. There is long-term upper ocean cooling and a decrease in salinity from summer to winter (Fig. 6), especially after mid-October. Kalmaegi reduced sea surface temperature by approximately 1.9 °C at its maximum, with a subsurface cold anomaly of approximately 1.1 °C at its maximum (Zhang et al., 2016) owing to its proximity to the typhoon track, where upper ocean temperature was primarily modulated by typhoon-induced mixing and upwelling (Zhang, 2023; Zhang et al., 2018). Vertical variations of temperature and salinity were also influenced by processes such as eddies, fronts, and flows (Liu et al., 2017; Lu et al., 2024), but these are not pursued further here. The downward propagation of warm or freshwater anomalies from the surface, along with the diurnal cycle of the near-surface mixed layer, can also be observed (Fig. 6) and partly analyzed in Zhang (2023).

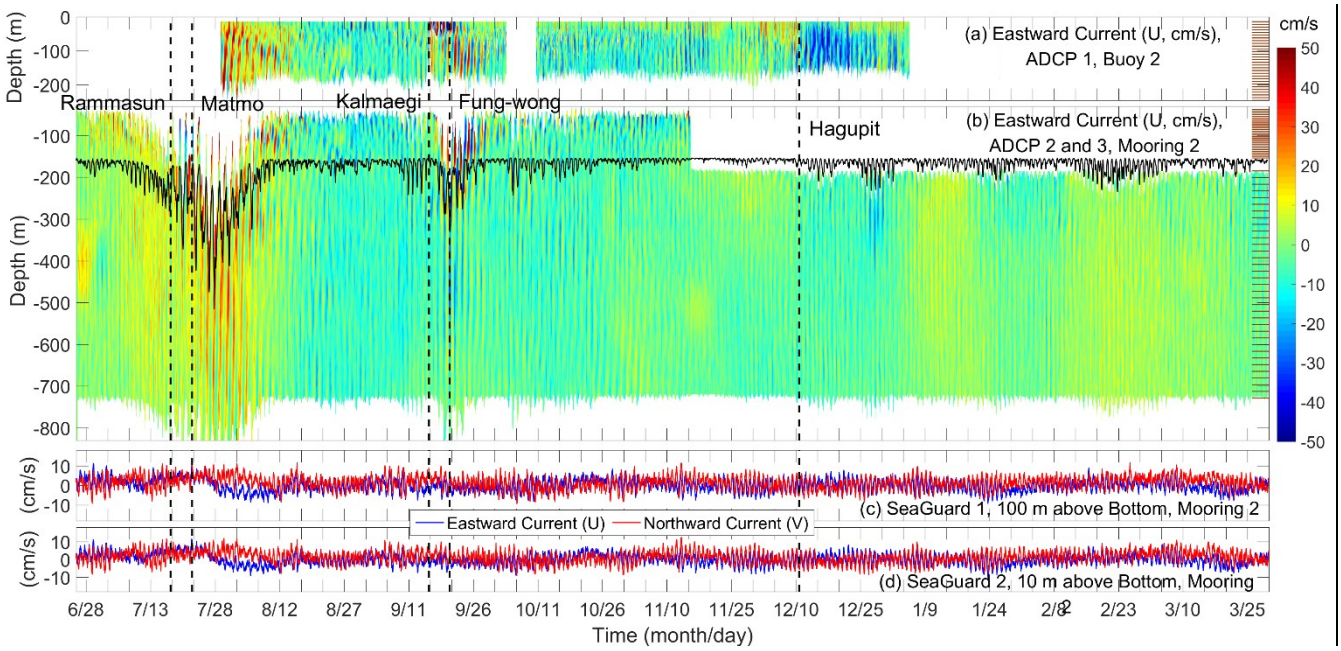

Figure 5: (a–b): Eastward currents (m/s) observed by the downward-looking 150 kHz ADCP at the buoy bottom (a), and the combination of upward-looking 300 kHz and downward-looking 75 kHz ADCP at the mooring (b). (c-d) Eastward (U) and northward (V) currents observed by SeaGuard current meter at 100 m (c) and 10 m (d) above the ocean bottom. Black solid line in (b) represents the vertical positions of ADCP 2 and 3. The vertical dashed lines represent the time when tropical cyclones closest to Buoy 2. The brown lines in (a) and (b) represent the initial depth of observation bins of the ADCPs.

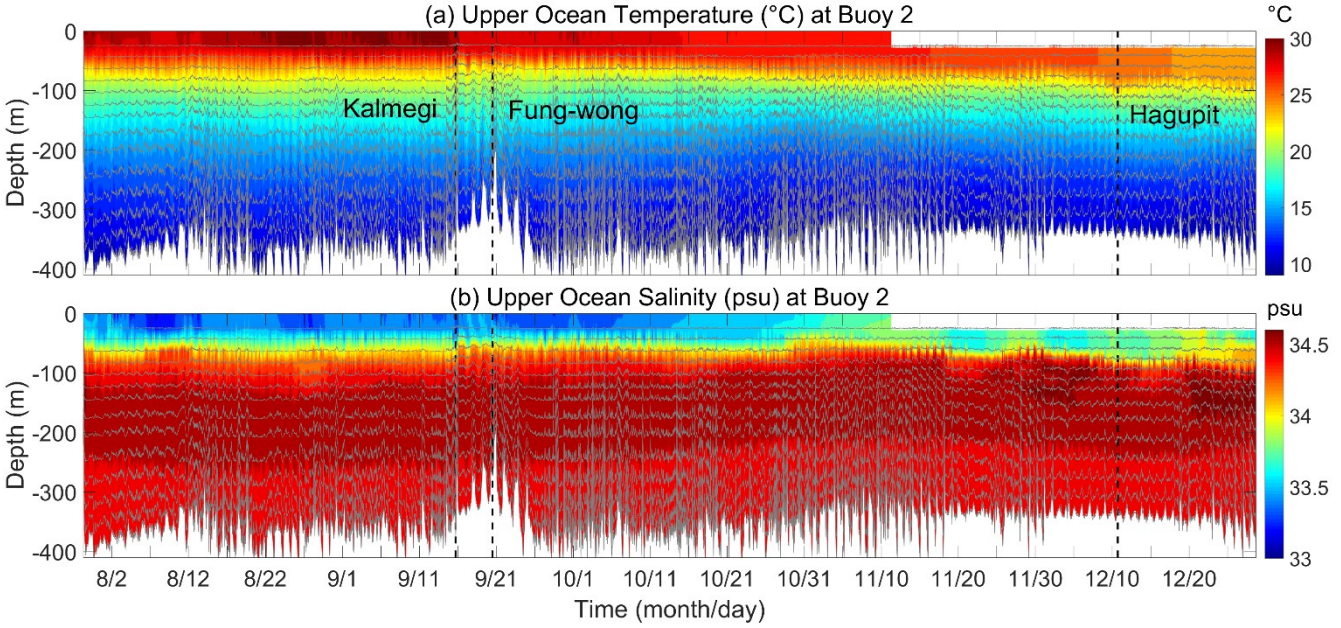

Figure 6: Upper ocean temperature (a, °C) and salinity (b, psu) observed by the chain of SBE-37 sensors at buoy 2. The vertical dashed lines indiate the time when tropical cyclones closest to Buoy 2. Gray lines represent the time variation of the depth of SBE-37 sensors.

3.3 Near bottom observation at mooring 1

The instruments at M1 differed from those at other moorings, so their observations are analyzed and discussed here. Three SBEs were deployed near the ocean bottom in order to check the homogeneity of the near-bottom layer. The variation of near-bottom pressure observed by the three SBEs at approximately 10 m, 30 m, and 50 m above the ocean bottom is very small (Fig. 7a), indicating minimal swing and tilt of the rope near the bottom of M1. The water pressure at approximately 10 m above the bottom was approximately 1710 dbar, corresponding to a depth of approximately 1690 m, indicating that the water depth of M1 was approximately 1700 m. The temperature varied from 2.5 °C to 2.7 °C, and salinity is close to 34.6 psu at the three SBEs (Fig. 7b,c). The temperature, salinity, and currents observed from the three SBEs and SeaGuards were very close, indicating a uniform near-bottom layer greater than 100 m (Fig. 7d). However, the current at 100 m above the bottom differed from the other two layers during 29 July to 12 August and 20 December to 13 December, when near-bottom flow also turned at M1, possibly influenced by super typhoons Rammasun and Hagupit (Fig. 7e).

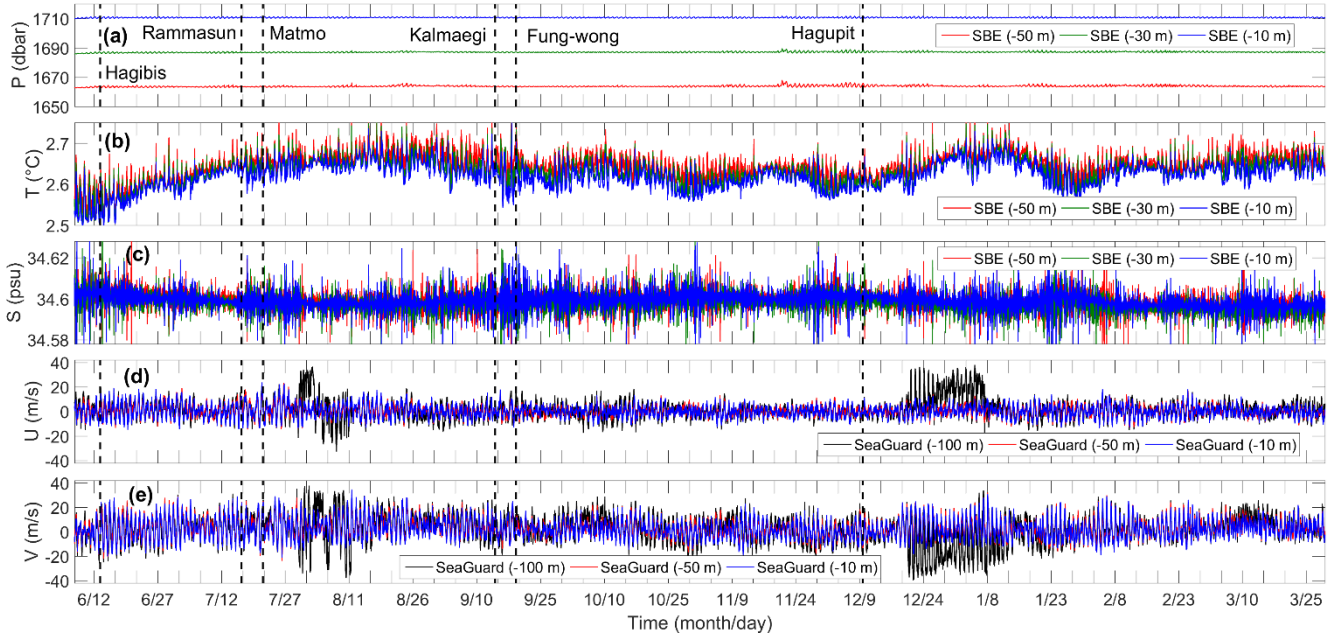

Figure 7: (a–c): Pressure (dbar a), temperature (°C b), and salinity (psu c) observed by the SBE-37 at the mooring at approximately 50 m (red), 30 m (green), and 10 m (blue) above the ocean bottom. (d-e) Eastward current (cm/s) and northward current observed by the SeaGuard current meter at the mooring at approximately 100 m (black), 50 m (red), and 10 m (blue) above the ocean bottom. The vertical dashed lines represent the time when tropical cyclones closest to Mooring 1.

3.4 Sea surface waves

Sea surface waves observed at B1 and B4 also merit further explanation. The variations of sea surface waves from the two wave gauges at B1 and B4 are similar (Fig. 8), indicating that the characteristic of the sea surface waves at the observation array were comparable. However, B4 showed more drastic variation of peak period than B1 with different mean wave direction

and wave spread during 14 to 20 July and near 26 July, which may due to the influence of tropical cyclones Habibis and Matmo. The observation at B1 were longer than B4, but with some miss recording near 1 August to 17 August.

Sea surface waves were mainly controlled by sea surface winds, e.g., monsoon and tropical cyclones. During the summer monsoon (before September), significant wave height was primarily <2 m, maximum wave height <3 m, peak period <10 s, and mean wave direction was close to 180° (northward). During the winter monsoon (after October), significant and maximum wave heights increased to >3 m and >5 m, respectively, as well as peak period > 10 s and mean wave direction nearly 90° (westward). Wave spread ranged from 20 to 80 throughout the observation period of the two wave gauges (Fig. 8e).Tropical cyclones strongly influenced local sea surface waves. Significant wave height increased to approximately 5 m, 10 m, and 3 m (Fig. 8a), while maximum wave height reached approximately 8 m, 15–18 m, and 5–6 m (Fig. 8b) due to the influence of tropical cyclones Rammasun, Kalmaegi, and Fung-wong, respectively. Sea surface wave height increased rapidly in one day, along with a clockwise rotation of mean wave direction and an increase in peak period, then returned to background conditions within approximately three days, with the mean wave direction rotating counterclockwise and a decrease in peak period (Fig. 8).

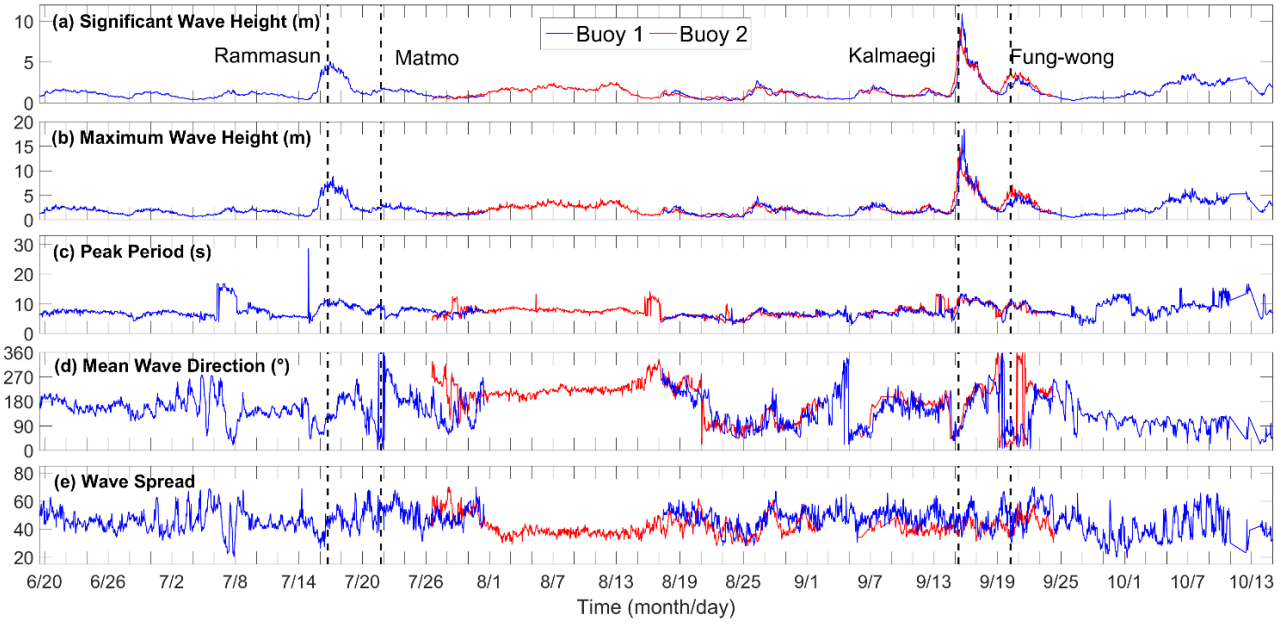

Figure 8: Significant wave height (a, m), maximum wave height (b, m), peak period (c, s), mean wave direction (d, °), and wave spread observed by the wave recorders at the bottom of buoys 1 (blue) and 4 (red). The vertical dashed lines represent the time when tropical cyclones closest to the moored array.

3.5 Observation at buoy 3

As the tether of B3 snapped on 15 September, causing the buoy to became adrift (Fig. 2), it is important to describe B3 observations in this section, which partly reflects the air-sea conditions in region B3 (Figs. 9 and 10).

The average and maximum wind speeds increased to approximately 20 m/s and 25 m/s, respectively, during Kalmaegi, with wind direction changing rapidly (Fig. 9a). The average and maximum wind speeds reached approximately 10 m/s during Fung-wong, with the wind direction rotating counterclockwise, as B3 was on the left side of the TC track (Fig. 9b). In October, the wind direction was primarily close to 0°, consistent with B2 (Fig. 4), indicating that the local region was controlled by the monsoon from nearly north to south. Rainfall was strong during Kalmaegi (approximately 250 mm) and Fung-wong (approximately 200 mm), accompanied by low air pressure (980 hPa and 1000 hPa), while there was little rainfall, and air pressure increased to more than 1100 hPa after 24 September (Fig. 9e,f). The diurnal variation of air pressure can also be found in the observation. Sea surface temperature continuously reduced from ~30°C to ~27.5°C and ~26.5°C after Kalmaegi and Fung-wong, and then recovered back to ~29°C in October (Fig. 10d). Note that surface air temperature (Fig. 9g) was 1-3 °C colder than sea surface temperature (Fig. 10d) during the observation, indicate that there was sensible heat flux from ocean to air in Autumn along the track of B3. Relative humidity was 85% to 100% during the influence of Kalmaegi and Fung-wong (14 to 25 September), and then continuously decreased to approximately 70% in October (Fig. 9h), consistent with the fact that the TC-induced cold wake results in reduced rainfall and sea surface humidity (e.g., Ma et al., 2020). Air visibility was approximately 10 km when B3 was deployed, then decreased to approximately 1 m due to cloud cover and adverse sea surface conditions from typhoon Kalmaegi, rapidly increased to approximately 16 km on 15 September due to the passage of the typhoon eye (Fig. 9i). Clear sky returned near 17 September, while subsequent tropical cyclone Fung-wong increased air visibility at B3 to approximately 16 km again on 20 September, lasting until 22–23 September.

B3 was the only buoy equipped with a radiometer. The maximum shortwave radiation observed by the upward sensor was approximately 1900 W/m^2 near noon (Fig. 10a), when solar radiation was strongest, significantly reduced by cloud cover from tropical cyclones from 13 to 23 September, and moderately reduced by local cloud cover in October. Conversely, the shortwave radiation observed by the downward sensor was much (one order) smaller than the upward shortwave radiation, indicating a minimal reflection of solar radiation. Similarly, the longwave radiation observed by the upward and downward sensors was close to 0 W/m^2 and approximately −50 W/m^2 (Fig. 10b), respectively, indicating that longwave radiation was primarily from the ocean to the atmosphere, with minimal contribution from the atmosphere to the ocean. The sea surface temperature (Fig. 10(d)) decreased from approximately 30 °C to approximately 27 °C after Kalmaegi, recovering to approximately 29 °C in October. The air temperature observed by the radiometer (Fig. 10c) followed a similar variation pattern with air temperature observed by meteorological sensors (Fig. 9a) and sea surface temperature (Fig. 10d), with significant diurnal variation. It is noteworthy that sea surface salinity (Fig. 10d) increased from approximately 33.5 psu to approximately 33.7 psu due to typhoon Kalmaegi, despite strong rainfall (Fig. 9e). The variation in sea surface salinity was consistent with the rain guage data, except for a decrease in salinity from 3 to 5 October. There were some recording errors of sea surface temperature and salinity after 5 October (Fig. 10d,e) with sudden change of the values. The SBE and RBR sensors were deployed at approximately 1.3 to 1.6 m from the surface, with pressures nearly 1.3 hPa–1.6 hPa (Fig. 10f). Chlorophyll observed by the RBR sensor (Fig. 10g) showed diurnal variation, increasing from approximately2 ug/L to approximately 2.5 ug/L after Kalmaegi and Fung-wong, then returning to approximately 2 ug/L afterward. Turbidity observed by the first sensor

(Fig. 10h) is more than 0.05 V before September 15, then decreased to approximately 0.005 V, making it difficult to determine whether the decrease is attributable to Kalmaegi, which made the sea surface cleaner, or damage to the turbidity sensor after B3's rope snapped. Conversely, turbidity observed by the second sensor (Fig. 10i) remained near 4.4569 throughout the observation period of B3 (Fig. 10i). Chromophoric dissolved organic matter (CDOM, Fig. 10j) gradually increased from 1.88 ppb in September to 2.1 ppb by mid-October.

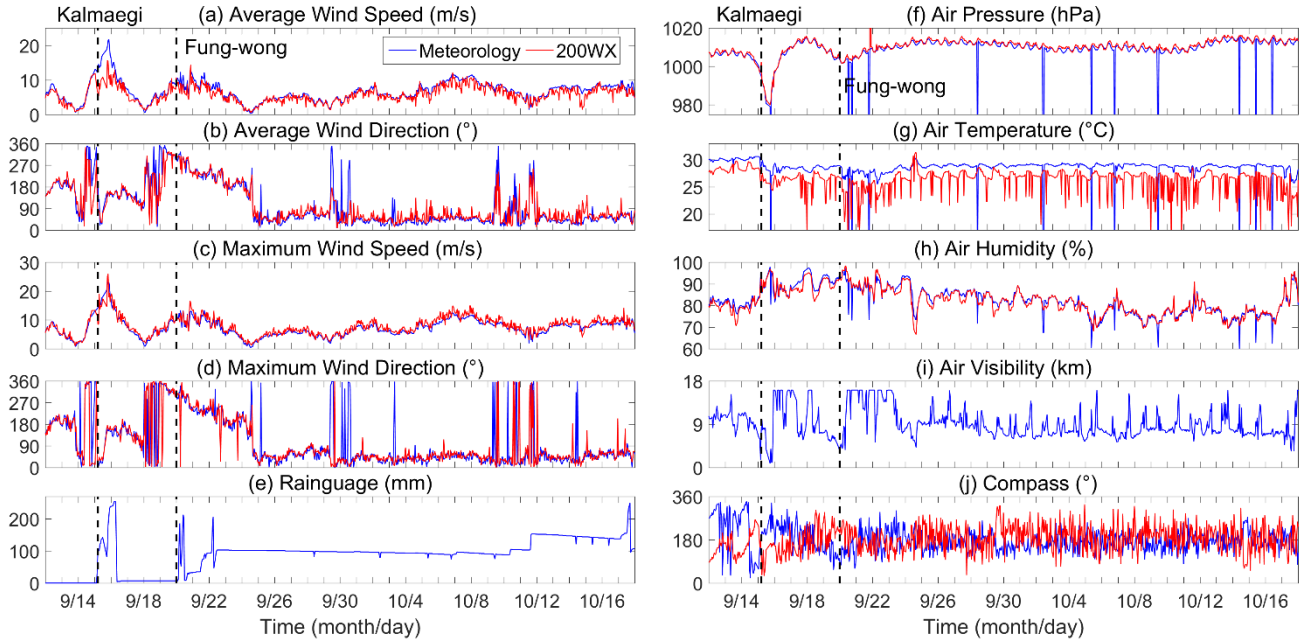

Figure 9: Similar to Figure 4 but for buoy 4. Note that (i) is air visibility (km) observed by a visibility meter located 4 m above the sea surface. The vertical dashed lines represent the time when tropical cyclones closest to the moored array.

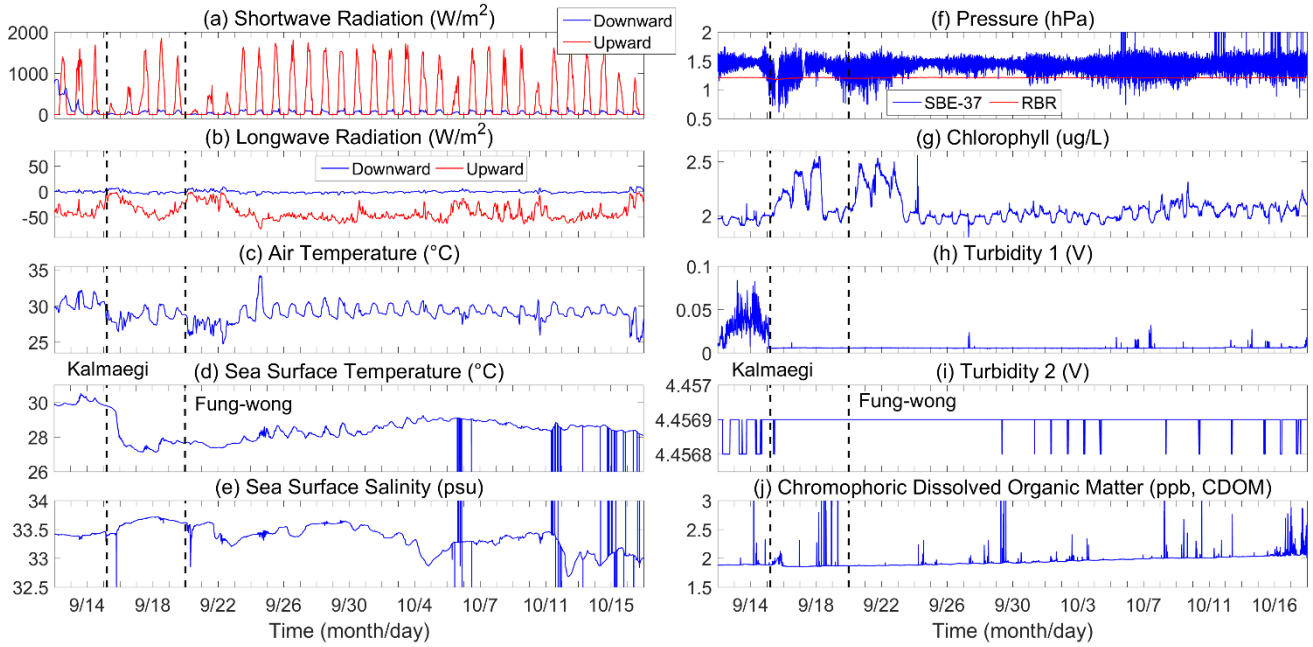

Figure 10: Observation at Buoy 3. (a–c): Shortwave radiation (a, W/m2) and longwave radiation (b, W/m2) observed by upward (red) and downward (blue) radiation sensors and the air temperature observed by the radiometer (c, °C) observed by the radiometer. (d–f): Sea surface temperature (f, °C), salinity (g, psu), and pressure (h, hPa, blue) observed by SBE-37, with pressure (h, hPa, red) observed by RBR sensors. (g–j): Chlorophyll (g, ug/L), turbidity observed by two sensors (g–h, V), and chromophoric dissolved organic matter (j, ppb, CDOM). Radiometer is located 4 m above the sea surface, while the SBE-37 and RBR sensors are at the bottom of buoy 3 (approximately 0 m). The vertical dashed lines represent the time when tropical cyclones closest to the moored array.

4. Data availability

All data are made publicly available through Zenodo repository with the address: https://zenodo.org/records/13827819 (Zhang et al. 2024). The data will also be publicly available at the website of the Southern Marine Science and Engineering Guangdong Laboratory (Zhuhai) (http://www.hellosea.org.cn/#/metadataDetail/en-US?detailId=8f32902492b84dc1a80f0f717a7c827e) if the manuscript published. This study provides a detailed description of the dataset, which includes a time series of sea surface meteorological elements, sea surface waves, ocean temperature, salinity, and currents collected from a moored array consisting of five buoys and four moorings during 2014–2015. Meteorological elements included wind, temperature, pressure, rain guage, and humidity data. In addition, data from the buoy at the center (B3) included sea surface visibility, radiation (shortwave and longwave), and biochemistry observations (chlorophyll, turbidity, and colored dissolved organic matter).

5 Conclusions

This study presents an observation dataset from a moored array consisting of five buoys (B1-B5) and four moorings (M1, M2, M4, M5) in the northern South China Sea during 2014–2015 (MASCS 1.0). The dataset includes measurements of sea surface meteorological data using two sets of instruments, sea surface waves recorded by a wave recorder, temperature and salinity from the surface to a depth of 400 m, and at 10 m and 50 m above the ocean bottom using conductivity, temperature, and depth (CTD) recorders. It also includes currents from the surface to a depth of 850 m measured by acoustic Doppler current profilers (ADCPs) and at 10 m, 50 m, and 100 m above the floor measured by current meters. Additional measurements were taken for sea surface radiation, air visibility, chlorophyll, turbidity and chromophoric dissolved organic matter at Buoy 3, which was located at the center of the moored array. The whole moored array started to be deployed at June 2014 while totally recovered at the end of 2015. Although some instruments as well as buoys broke down or were lost during observation, resulting in no data recovery or data deficiencies, this dataset is valuable for further studies to uncover air-sea interactions and oceanic processes in the northern South China Sea.

For example, tropical cyclones Hagibis in June, Rammasun and Matmo in July, Kalmaegi and Fung-wong in September, and Hagupit in December 2014 traveled over the South China Sea and influenced the time series of the observations. The tropical cyclones increased sea surface wind speed, enhanced sea surface wave height and near-surface ocean currents, cooled sea surface water and air temperature, induced near-inertial waves as well as near-bottom currents. The moored array also experienced a transition from the summer to winter monsoons, with prevailing nearly south wind (approximately 200°) and wave (approximately 180°) with sea surface significant wave height <2 m and peak period <10 s from late July to mid-August, then shifted to nearly northeast wind (approximately 20°–80°) and east wave (approximately 90°) with sea surface significant wave height >3 m and peak period <10 s after October. In addition, ocean data may have recorded multiscale air-sea interactions and ocean processes, such as air-sea heat and momentum fluxes, ocean tides, internal waves, seasonal variations in temperature, salinity, and flows, as well as background processes, such as mesoscale eddies and local circulations.

The data has already been used for the analysis of the air-sea and ocean variations on the moored array (Quan et al., 2022; He et al., 2024), validation of ocean (Zhang et al., 2016; Liu et al., 2020; Lu et al., 2023) and air-sea coupled (Wu et al., 2020; Lim Kam Sian et al., 2020; Liu et al., 2024) model simulation, check the parameterization of air-sea surface flux (Zhang et al., 2020; Liu et al., 2024), investigate the mechanisms and theory of ocean response to tropical cyclones (Hong et al., 2022; Zhang 2023). The dataset has the potential for further studies in these fields, while may also be used for other fields such as data reanalysis and assimilations.

Author Contributions. The dataset is made and the whole manuscript is written by HZ, the whole observation project is designed by DC, the flow of the manuscript is revised by TL and DT, the dataset is optimized by MH, QL and JL.

Competing Interests. The contact author has declared that none of the authors has any competing interests.

Financial support. This work has been supported by the National Key R&D Program of China (2023YFF0805300), the Key R&D Program of Zhejiang Province (2024C03257), the Scientific Research Fund of the Second Institute of Oceanography, MNR (JG2309, QNYC2401), the Project supported by Innovation Group Project of Southern Marine Science and Engineering Guangdong Laboratory (Zhuhai) (316323005), the National Natural Science Foundation of China (42227901, 42176015, 42106008), the National Basic Research Program of China (2013CB430300), the Project supported by Southern Marine Science and Engineering Guangdong Laboratory (Zhuhai) (SML2021SP207, SML2021SP102, SML2022SP401), the MEL Visiting Fellowship (MELRS2303), the Zhejiang Provincial Natural Science Foundation of China (LY24D060003), and the Global Change and Air-Sea Interaction II Program (GASI-01-WPAC-STspr), the Open Project of Fujian Provincial Meteorological Administration (2022K02), and the Zhejiang Provincial Natural Science Foundation of China (2022J011078). This research is also supported by the Key Laboratory of Polar Atmosphere-ocean-ice System for Weather and Climate, Ministry of Education, as well as the CMA-FDU Joint Laboratory of Maine Meteorology.

References

Alford, M. H., Peacock, T., MacKinnon, J. A., Nash, J. D., Buijsman, M. C., Centurioni, L. R., Chao, S. Y., Chang, M. H., Farmer, D. M., Fringer, O. B., Fu, K. H., Gallacher, P. C., Graber, H. C., Helfrich, K. R., Jachec, S. M., Jackson, C. R., Klymak, J. M., Ko, D. S., Jan, S., Johnston, T. M., Legg, S., Lee, I. H., Lien, R. C., Mercier, M. J., Moum, J. N., Musgrave, R., Park, J. H., Pickering, A. I., Pinkel, R., Rainville, L., Ramp, S. R., Rudnick, D. L., Sarkar, S., Scotti, A., Simmons, H. L., St Laurent, L. C., Venayagamoorthy, S. K., Wang, Y. H., Wang, J., Yang, Y. J., Paluszkiewicz, T., and Tang, T. Y.: The formation and fate of internal waves in the South China Sea, Nature, 521, 65–69, doi:10.1038/nature14399, 2015.

Cai, Z., Gan, J., Liu, Z., Hui, C. R., and Li, J.: Progress on the formation dynamics of the layered circulation in the South China Sea, Prog. Oceanogr, 181, 102246, doi:10.1016/j.pocean.2019.102246, 2020.

Chen, W., Hu, P., and Huangfu, J.: Multi-scale climate variations and mechanisms of the onset and withdrawal of the South China Sea summer monsoon, Sci. China Earth Sci., 65, 1030–1046, doi:10.1007/s11430-021-9902-5, 2022.

Chen, W., Zhang, R., Wu, R., Wen, Z., Zhou, L., Wang, L., Hu, P., Ma, T., Piao, J., Song, L., Wang, Z., Li, J., Gong, H., Huangfu, J., and Liu, Y.: Recent Advances in Understanding Multi-scale Climate Variability of the Asian Monsoon, Adv. Atmos. Sci., 40, 1–28, doi:10.1007/s00376-023-2266-8, 2023.

Guan, S., Jin, F. F., Tian, J., Lin, II, Pun, I. F., Zhao, W., Huthnance, J., Xu, Z., Cai, W., Jing, Z., Zhou, L., Liu, P., Zhang, Y., Zhang, Z., Zhou, C., Yang, Q., Huang, X., Hou, Y., and Song, J.: Ocean internal tides suppress tropical cyclones in the South China Sea, Nat. Commun., 15, 3903, doi:10.1038/s41467-024-48003-y, 2024.

He, Y., Lin, X., Han, G., Liu, Y., and Zhang, H.: The different dynamic influences of Typhoon Kalmaegi on two pre-existing anticyclonic ocean eddies, Ocean Sci., 20, 621–637, doi:10.5194/os-20-621-2024, 2024.

Hong, W., Zhou, L., Xie, X., Zhang, H., and Liang, C.: Modified parameterization for near-inertial waves, Acta Oceanol. Sin., 41, 41-53, doi:10.1007/s13131-022-2012-6, 2022.

Jilan, S.: Overview of the South China Sea circulation and its influence on the coastal physical oceanography outside the Pearl River Estuary, Cont. Shelf Res., 24, 1745–1760, doi:10.1016/j.csr.2004.06.005, 2004.

Li, J., Zhou, C., Li, M., Zheng, Q., Li, M., and Xie, L.: A case study of continental shelf waves in the northwestern South China Sea induced by winter storms in 2021, Acta Oceanol. Sin., 43, 59–69, doi:10.1007/s13131-023-2150-5, 2024.

Lim Kam Sian, K. T. C., Dong, C., Liu, H., Wu, R., and Zhang, H.: Effects of Model Coupling on Typhoon Kalmaegi (2014) Simulation in the South China Sea, Atmosphere, 11, 432, doi:10.3390/atmos11040432, 2020.

Lin, J., Fang, S., Xu, W., Ni, S., Zhang, H., and Yang, T.: Multi-instrument observations of microseisms generated by typhoon Kalmaegi (2014) over the Northwestern Pacific, Earth Planet. Sci. Lett., 594, 117746, doi:10.1016/j.epsl.2022.117746, 2022.

Liu, L., Wang, G., Zhang, Z., and Wang, H.: Effects of drag coefficients on surface heat flux during Typhoon Kalmaegi (2014), Adv. Atmos. Sci., 39, 1501-1518, doi:10.1007/s00376-022-1285-1, 2022.Liu, F., Zhang, H., Ming, J., Zheng, J., Tian, D., and Chen, D.: Importance of Precipitation on the Upper Ocean Salinity Response to Typhoon Kalmaegi (2014), Water, 12, 614, doi:10.3390/w12020614, 2020.

Liu, F., Toumi, R., Zhang, H., Chen, D.: Impact of Precipitation on Ocean Responses during Tropical Cyclone. J. Phys. Oceanogr., 54, 895–909, doi:10.1175/jpo-d-23-0138.1, 2024.

Liu, Q., Kaneko, A., and Jilan, S.: Recent Progress in Studies of the South China Sea Circulation, J. Oceanogr., 64, 753–762, doi:10.1007/s10872-008-0063-8, 2008.

Liu, S.-S., SUN, L., Wu, Q., and Yang, Y.-J.: The responses of cyclonic and anti-cyclonic eddies to typhoon forcing: the vertical temperature-salinity structure changes associated with the horizontal convergence/divergence, J. Geophys. Res. Oceans, 122, 4974–4989, doi:10.1002/2017JC012814, 2017.

Lu, X., Dong, C., Xu, Z., Yang, J., Zhang, H., Wang, D., and Chen, D.: Effects of numerical model's horizontal resolution on the vertical transport of near-inertial energy, Deep-Sea Res. II, 207, 105223, doi:10.1016/j.dsr2.2022.105223, 2023.

Lu, X., Yu, H., Ying, M., Zhao, B., Zhang, S., Lin, L., Bai, L., and Wan, R.: Western North Pacific Tropical Cyclone Database Created by the China Meteorological Administration, Adv. Atmos. Sci., 38, 690–699, doi:10.1007/s00376-020-0211-7, 2021.

Lu, X., Dong, C., Zhang, H., Lim Kam Sian, K. T. C., Yang, J., Xu, Z., Li, G., Wang, Q., Cao, Q., You, Z., and Sommeria, J.: Observational Analysis of Vertical Heat Flux Caused by Typhoon-Induced Near-Inertial Waves Under the Modulation of Mesoscale Eddies, J. Geophys. Res. Oceans, 129, e2024JC021053, doi:10.1029/2024jc021053, 2024.

Ma, Z., Fei, J., Lin, Y., and Huang, X.: Modulation of Clouds and Rainfall by Tropical Cyclone's Cold Wakes, Geophys. Res. Lett., 47, e2020GL088873, doi:10.1029/2020gl088873, 2020.

Nan, F., Xue, H., and Yu, F.: Kuroshio intrusion into the South China Sea: A review, Prog. Oceanogr., 137, 314–333, doi:10.1016/j.pocean.2014.05.012, 2015.

Qi, M., Han, B., Yang, Q., Wu, R., Liu, C., Zhang, G., Zhang, X., Zhou, H., Chen, J., and Chen, D.: Sea Surface Energy Fluxes' Response to the Quasi-Biweekly Oscillation: A Case Study in the South China Sea, Geophys. Res. Lett., 50, doi:10.1029/2023gl104288, 2023.

Quan, Q., Liu, Z., Yang, Y., Cai, Z., Zhang, H., and Liu, X.: Characterization of intraseasonal fluctuations in the abyssal South China Sea: An insight into the energy pathway, Prog. Oceanogr., 206, 102829, doi: 10.1016/j.pocean.2022.102829, 2022.

Shan, K., Chu, P.-S., and Yu, X.: Interdecadal Change of Tropical Cyclone Translation Speed during Peak Season in South China Sea: Observed Evidence, Model Results, and Possible Mechanism, J. Clim., 36, 4531–4541, doi:10.1175/jcli-d-22-0704.1, 2023.

Song, X., Wang, X., Cai, W., and Xie, X.: Observed Air–Sea Turbulent Heat Flux Anomalies during the Onset of the South China Sea Summer Monsoon in 2021, Mon. Weather Rev., 151, 2443–2464, doi:10.1175/mwr-d-22-0314.1, 2023.

Tan, K., Xie, L., Bai, P., Zheng, Q., Li, J., Xu, Y., and Li, M.: Modulation Effects of Mesoscale Eddies on Sea Surface Wave Fields in the South China Sea Derived From a Wave Spectrometer Onboard the China-France Ocean Satellite, J. Geophys.

Res. Oceans, 128, doi:10.1029/2021jc018088, 2023.

Wang, Q., Zhang, B., Zeng, L., He, Y., Wu, Z., and Chen, J.: Properties and Drivers of Marine Heat Waves in the Northern South China Sea, J. Phys. Oceanogr., 52, 917–927doi:10.1175/jpo-d-21-0236.1, 2022.

Wang, Q., Zeng, L., Shu, Y., Li, J., Chen, J., He, Y., Yao, J., Wang, D., and Zhou, W.: Energetic Topographic Rossby Waves in the northern South China Sea, J. Phys. Oceanogr., 49, 2697–2714, doi:10.1175/JPO-D-18-0247.1, 2019.

Wu, R., Zhang, H., and Chen, D.: Effect of Typhoon Kalmaegi (2014) on northern South China Sea explored using Muti-platform satellite and buoy observations data, Prog. Oceanogr., 180, 102218, doi:10.1016/j.pocean.2019.102218, 2020.

Xie, X., Liu, Q., Zhao, Z., Shang, X., Cai, S., Wang, D., and Chen, D.: Deep Sea Currents Driven by Breaking Internal Tides on the Continental Slope, Geophys. Res. Lett., 45, 6160–6166, doi:10.1029/2018GL078372, 2018.

Yang, Y., Wang, D., Wang, Q., Zeng, L., Xing, T., He, Y., Shu, Y., Chen, J., and Wang, Y.: Eddy-Induced Transport of Saline Kuroshio Water Into the Northern South China Sea, J. Geophys. Res. Oceans, 124, 6673–6687, doi:10.1029/2018jc014847, 2019.

Ying, M., Zhang, W., Yu, H., Lu, X., Feng, J., Fan, Y., Zhu, Y., and Chen, D.: An Overview of the China Meteorological Administration Tropical Cyclone Database, J. Atmos. Oceanic Tech., 31, 287–301, doi:10.1175/jtech-d-12-00119.1, 2014.

Zhang, H.: Modulation of Upper Ocean Vertical Temperature Structure and Heat Content by a Fast-Moving Tropical Cyclone, J. Phys. Oceanogr., 53, 493–508, doi:10.1175/JPO-D-22-0132.1, 2023.

Zhang, H., Chen, D., Tongya, L., Tian, D., He, M., Li, Q., Wei, G., and Liu, J.: A Moored Array Observation Dataset for Air-Sea·Surface, Upper and Bottom Ocean in the Northern South China Sea during 2014-2015 (MASCS 1.0) [Data set]. Zenodo. doi: 10.5281/zenodo.13827819, 2024.

Zhang, H., Chen, D., Zhou, L., Liu, X., Ding, T., and Zhou, B.: Upper ocean response to typhoon Kalmaegi (2014), J. Geophys. Res. Oceans, 121, 6520–6535, doi:10.1002/2016jc012064, 2016.

Zhang, H., Liu, X., Wu, R., Chen, D., Zhang, D., Shang, X., Wang, Y., Song, X., Jin, W., Yu, L., Qi, Y., Tian, D., and Zhang, W.: Sea surface current response patterns to tropical cyclones, J. Marine Syst., 208, 103345, doi:10.1016/j.jmarsys.2020.103345, 2020.

Zhang, H., Wu, R., Chen, D., Liu, X., He, H., Tang, Y., Ke, D., Shen, Z., Li, J., Xie, J., Tian, D., Ming, J., Liu, F., Zhang, D., and Zhang, W.: Net Modulation of Upper Ocean Thermal Structure by Typhoon Kalmaegi (2014), J. Geophys. Res. Oceans, 123, 7154–7171, doi:10.1029/2018JC014119, 2018.